

Chiral vibrations and collective bands in $^{104,106}\text{Mo}$

B. M. Musangu^{1,2}, E. H. Wang¹, J. H. Hamilton¹, S. Jehangir³, G. H. Bhat^{4,5}, J. A. Sheikh^{5,6}, S. Frauendorf⁷,
 C. J. Zachary⁸, J. M. Eldridge¹, A. V. Ramayya¹, A. C. Dai⁸, F. R. Xu⁸, J. O. Rasmussen⁹, Y. X. Luo^{1,9},
 G. M. Ter-Akopian¹⁰, Yu. Ts. Oganessian¹⁰ and S. J. Zhu¹¹

¹*Department of Physics and Astronomy, Vanderbilt University, Nashville, Tennessee 37235, USA*

²*Department of Physics, Furman University, Greenville, South Carolina 29613, USA*

³*Department of Nuclear and Atomic Physics, Tata Institute of Fundamental Research, Mumbai 400 005, India*

⁴*Department of Physics, SP College Srinagar 190 001, India*

⁵*Cluster University Srinagar, Jammu and Kashmir, Gogji Bagh 190 008, India*

⁶*Department of Physics, University of Kashmir, Srinagar 190 006, India*


⁷*Department of Physics, University of Notre Dame, Notre Dame, Indiana 46556, USA*

⁸*Department of Physics, Peking University, Beijing 100871, People's Republic of China*

⁹*Lawrence Berkeley National Laboratory, Berkeley, California 94720, USA*

¹⁰*Joint Institute for Nuclear Research, RU-141980 Dubna, Russian Federation*

¹¹*Department of Physics, Tsinghua University, Beijing 100084, People's Republic of China*

 (Received 23 July 2020; revised 24 September 2021; accepted 24 November 2021; published 22 December 2021)

High spin states of the neutron-rich ^{104}Mo nucleus have been reinvestigated by analyzing the γ rays in the spontaneous fission of ^{252}Cf with Gammasphere. Both γ - γ - γ and γ - γ - γ - γ coincidence data were analyzed. A new $\Delta I = 1$ band has been discovered with a tentative 5^- band head, and is proposed to form a class of chiral vibrational doublets with another 4^- band previously found. Angular correlation measurements have been performed to determine the spins and parities. A new 3^- level has been added to one of the chiral doublet bands in ^{106}Mo . The origin of the chiral doublet bands in $^{104,106}\text{Mo}$ is interpreted as a neutron $h_{11/2}$ particle and mixed $d_{5/2}$, $g_{7/2}$ hole coupled to the short and long axis, respectively. Triaxial projected shell model calculations have been performed for the chiral doublet bands in $^{104,106}\text{Mo}$. The results show reasonably good agreement with the experimental data.

DOI: [10.1103/PhysRevC.104.064318](https://doi.org/10.1103/PhysRevC.104.064318)

I. INTRODUCTION

In nuclear structure research, chirality, or handedness, is the study of left- and right- handed symmetry in a nucleus which yields a pair of nearly degenerate $\Delta I = 1$ rotational bands. Such phenomenon was predicted theoretically in 1997 [1]. Chiral doublets occur in triaxial nuclei when the angular momentum has components along all the three principal axes. Since then, chiral nuclei have been suggested experimentally in $A \approx 80$ [2,3], $A \approx 100$ [4–16], $A \approx 130$ [17–20], and $A \approx 190$ [21,22] mass regions. The soft triaxial ^{106}Mo was suggested to have chiral doublet bands [9], where chirality is generated by a neutron $h_{11/2}$ particle and mixed $d_{5/2}$, $g_{7/2}$ hole coupled to the short and long axis, respectively. The same chiral configurations were identified in $^{108,110,112}\text{Ru}$ [12].

The ^{104}Mo nucleus, as well as ^{106}Mo , have one- and two-phonon gamma vibrational bands, which indicate the softness with respect to triaxial deformations [23,24]. In these soft nuclei, nuclear shapes may be driven to stable triaxiality due to the excitation of quasiparticles [25,26]. In the present work, we find the candidates for chiral doublet bands in ^{104}Mo with more degenerate energies for states of the same spin

(≈ 60 keV) than in ^{106}Mo (≈ 100 to 140 keV) [9]. Close agreement of the levels of the same spin states in the two bands is a fingerprint for chiral bands.

II. EXPERIMENTAL METHOD AND RESULT

The experiment was carried out at the Lawrence Berkeley National Laboratory (LBNL). A $62 \mu\text{Ci}$ ^{252}Cf source was sandwiched between two 10 mg/cm^2 Fe foils and was mounted in a 7.62-cm-diameter polyethylene ball. By using 101 Ge detectors of Gammasphere, high statistics of prompt γ rays emitted in spontaneous fission of ^{252}Cf were detected. The data were sorted into 5.7×10^{11} γ - γ - γ and higher fold and 1.9×10^{11} γ - γ - γ - γ and higher fold γ coincident events. The fourfold data are extremely helpful in clarifying new transitions and contamination. These data were analyzed by the RADWARE software package [27]. The angular resolution of Gammasphere is used to obtain γ - γ angular correlations [28]. More details of this experiment can be found in Ref. [29].

The partial level schemes of $^{104,106}\text{Mo}$ obtained in the present work are shown in Figs. 1 and 2. Both of the level scheme figures are split into upper and lower parts in order to

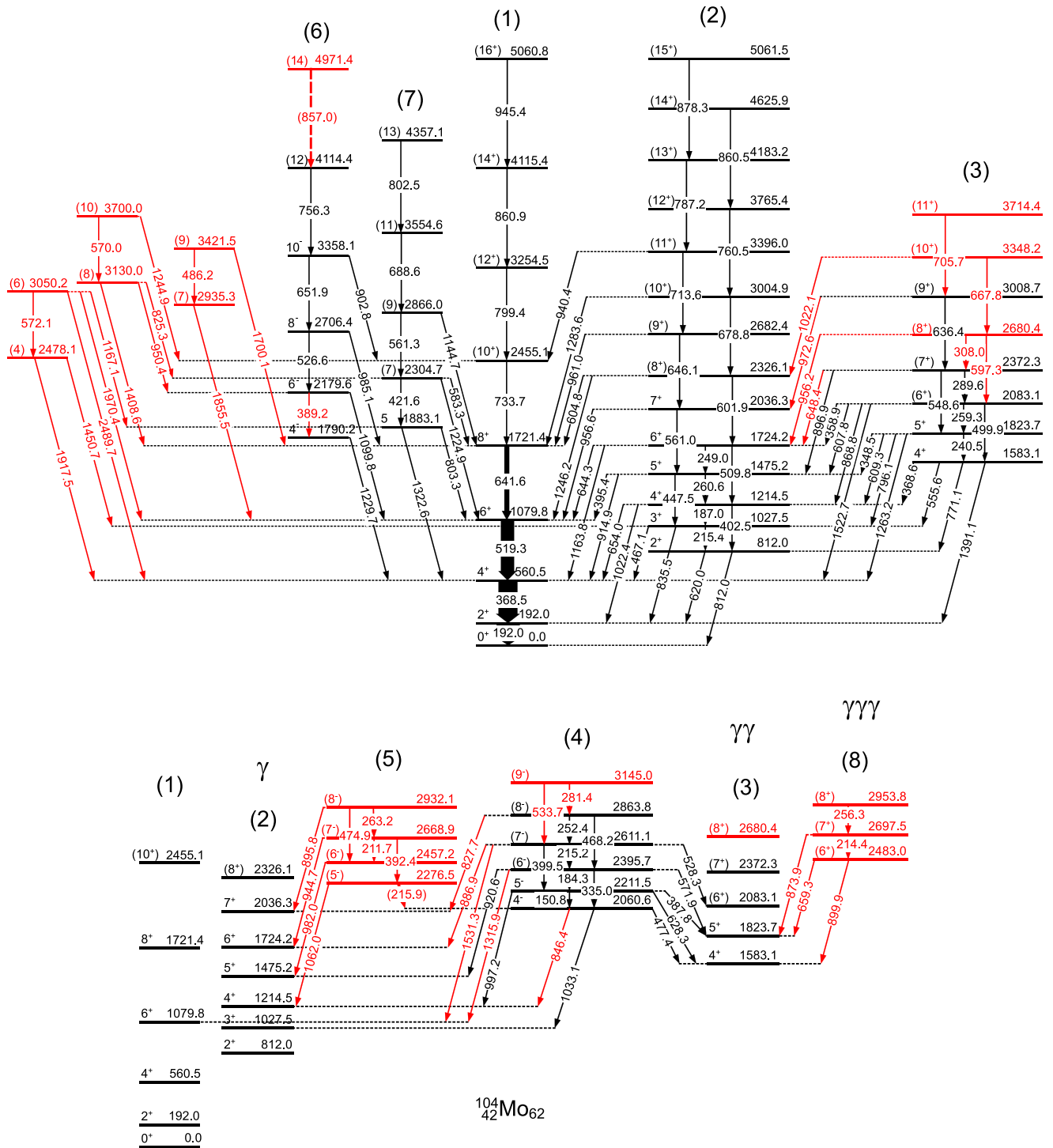


FIG. 1. Partial level scheme of ^{104}Mo obtained in the current work. New levels and transitions are labeled in red.

clarify the transitions and band structures. The previous high spin studies of these nuclei [24,30,31] have been extended by new transitions, new levels, and some corrections to the previous transitions. Level and gamma-ray energies together with gamma-ray intensities of $^{104,106}\text{Mo}$ are listed in Tables I and II, respectively. Detailed γ -ray spectra evidences, new

transitions, new levels, and band structures are discussed below.

A. ^{104}Mo spectra

In ^{104}Mo , the ground-state band (1) and γ -vibrational band (2) have been confirmed. The two-phonon γ -vibrational band

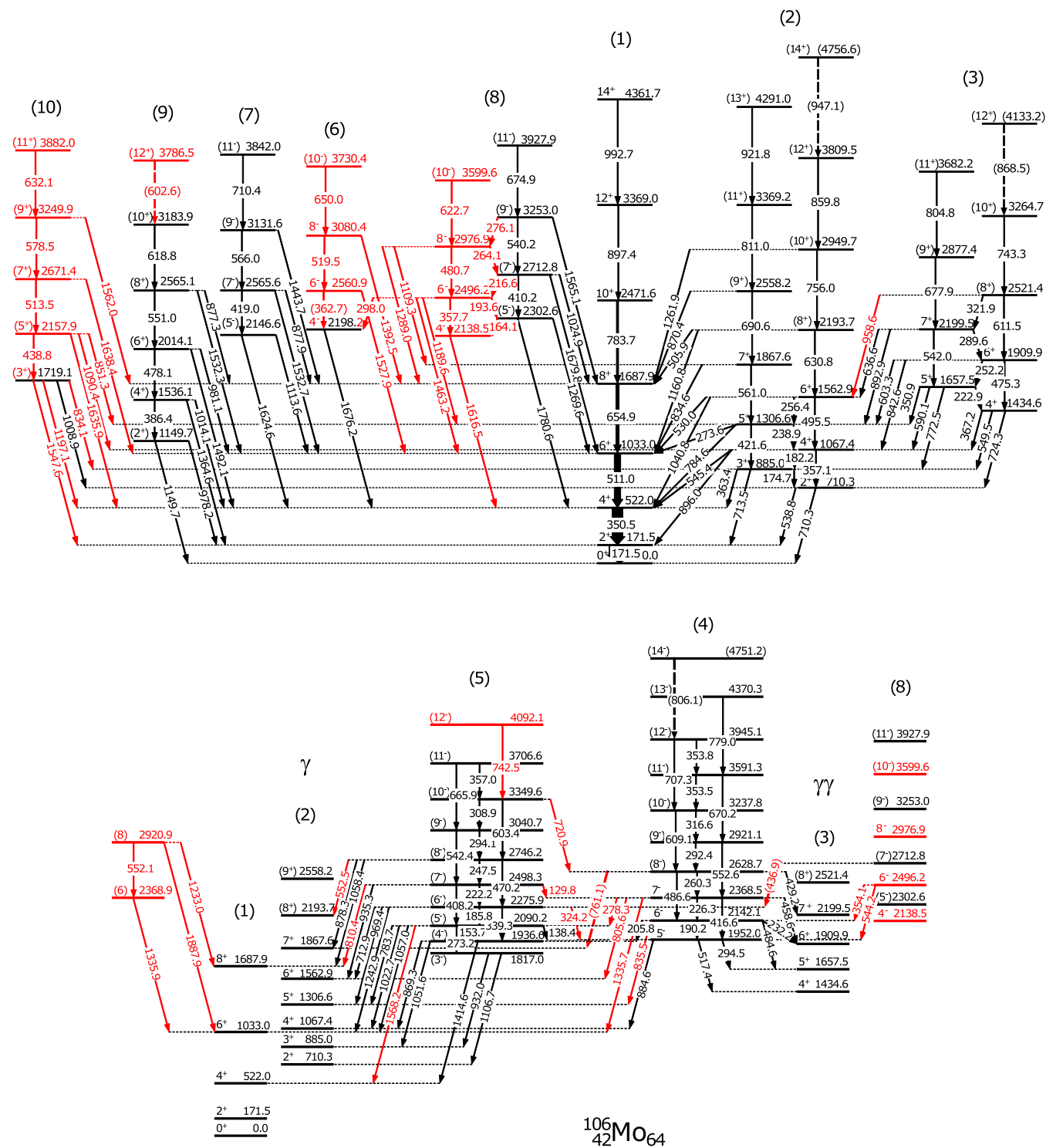


FIG. 2. Partial level scheme of ^{106}Mo obtained in the current work. New levels and transitions are labeled in red. In the lower part of this figure, we do not show all the transitions from band (8).

(3) levels have been extended and reassigned. In Ref. [31], the 8^+ to 6^+ transition of the two-phonon γ -vibrational band was reported as 601.6 keV. This transition is replaced by a 597.3 keV transition in the current work. Figure 3 shows γ -ray coincidence spectrum by gating on the 499.9 and 771.1 keV transitions. In this spectrum, the 597.3 and 667.8 keV $E2$ new transitions and the 308.0 keV $M1$ new transition in band (3)

can be seen. The previous reported 601.6 keV in Ref. [31] lies on the 600 keV neutron platform on the right of the 597.3 keV peak in Fig. 3.

Figure 4 depicts the high-energy part of the spectra by gating on the (a) 192.0 keV ground-state band transition and 914.9 keV depopulating the 1475 keV 5^+ level of band (2), and (b) 835.5 keV transition depopulating the 3^+ level of band

TABLE I. Level energies and γ -ray energies of ^{104}Mo obtained in the current work. Here, E_i , E_f , E_γ , I_γ and B correspond to initial level energy, final level energy, γ -ray energy, γ -ray intensity, and band number, respectively. The γ -ray intensities are normalized to the 192.0 keV one. New levels and transitions are labeled with an asterisk.

Initial level			Final level				
E_i (keV)	J^π	B	E_γ (keV)	I_γ	E_f (keV)	J^π	B
0.0	0+	1					
192.0	2+	1	192.0	100(5)	0.0	0+	1
560.5	4+	1	368.5	83(4)	192.0	2+	1
812.0	2+	2	620.0	6.2(3)	192.0	2+	1
			812.0	5.1(3)	0.0	0+	1
1027.5	3+	2	215.4	<0.4	812.0	2+	2
			467.1	1.0(1)	560.5	4+	1
			835.5	9.8(5)	192.0	2+	1
1079.8	6+	1	519.3	53(3)	560.5	4+	1
1214.5	4+	2	402.5	1.0(1)	812.0	2+	2
			187.0	<0.18	1027.5	3+	2
			654.0	6.2(3)	560.5	4+	1
			1022.4	3.8(2)	192.0	2+	1
1475.2	5+	2	260.6	0.27(6)	1214.5	4+	2
			395.4	0.18(6)	1079.8	6+	1
			447.5	2.7(1)	1027.5	3+	2
			914.9	6.4(3)	560.5	4+	1
1583.1	4+	3	368.6	2.0(2)	1214.5	4+	2
			555.6	2.7(2)	1027.5	3+	2
			771.1	6.1(3)	821.0	2+	2
			1391.0	0.24(3)	192.0	2+	1
1721.4	8+	1	641.6	2.2(1)	1079.8	6+	1
1724.2	6+	2	249.0	0.4(1)	1475.2	5+	2
			509.8	2.9(2)	1214.5	4+	2
			644.3	1.8(1)	1079.8	6+	1
			1163.8	2.2(1)	560.5	4+	1
1790.2	4-	6	1229.7	0.77(5)	560.5	4+	1
1823.7	5+	3	240.5	3.9(4)	1583.1	4+	3
			348.5	0.58(6)	1475.2	5+	2
			609.3	1.4(1)	1214.5	4+	2
			796.1	2.9(2)	1027.5	3+	2
			1263.2	0.40(3)	560.5	4+	1
1883.1	5	7	803.3	1.2(1)	1079.8	6+	1
			1322.6	1.7(1)	560.5	4+	1
2036.3	7+	2	561.0	4.0(3)	1475.2	5+	2
			956.6	2.1(1)	1079.8	6+	1
2060.6	4-	4	477.4	2.2(2)	1583.1	4+	3
			846.4*	0.52(8)	1214.5	4+	2
			1033.1	0.05(1)	1027.5	3+	2
2083.1	(6+)	3	259.3	1.1(1)	1823.7	5+	3
			358.9	0.6(1)	1724.2	6+	2
			499.9	1.5(1)	1583.1	4+	3
			607.8	0.63(4)	1475.2	5+	2
			868.8	0.81(6)	1214.5	4+	2
			1522.7	0.38(2)	560.5	4+	1
2179.6	6-	6	389.2*	0.021(2)	1790.2	4-	6
			1099.8	1.6(1)	1079.8	6+	1
2211.5	5-	4	150.8	1.6(2)	2060.6	4-	4
			387.8	1.7(2)	1823.7	5+	3
			628.3	1.3(1)	1583.1	4+	3
			997.2	0.34(3)	1214.5	4+	2
2276.5*	(5-)	5	(215.9)*		2060.6	4-	4
			1062.0*	0.11(2)	1214.5	4+	2

TABLE I. (Continued.)

Initial level								Final level		
E_i (keV)	J^π	B	E_γ (keV)	I_γ	E_f (keV)	J^π	B			
2304.7	(7)	7	421.6	1.4(1)	1883.1	5	7			
			583.3	2.2(1)	1721.4	8+	1			
			1224.9	2.8(1)	1079.8	6+	1			
2326.1	(8+)	2	601.9	3.3(3)	1724.2	6+	2			
			604.8	0.7(1)	1721.4	8+	1			
			1246.2	0.93(5)	1079.8	6+	1			
2372.3	(7+)	3	289.6	1.3(3)	2083.1	(6+)	3			
			548.6	1.4(2)	1823.7	5+	3			
			648.4*	0.41(9)	1724.2	6+	2			
			896.9	0.20(4)	1475.2	5+	2			
2395.7	(6-)	4	184.3	0.75(4)	2211.5	5-	4			
			335.0	0.30(2)	2060.6	4-	4			
			571.9	0.8(2)	1823.7	5+	3			
			920.6	0.25(2)	1475.2	5+	2			
			1315.9*	0.24(1)	1079.8	6+	1			
			733.7	7.8(4)	1721.4	8+	1			
2455.1	10+	1	733.7	7.8(4)	1721.4	8+	1			
2457.2*	(6-)	5	982.0*	0.22(2)	1475.2	5+	2			
2478.1*	(4)		1450.7*	0.22(1)	1027.5	3+	2			
2483.0*	(6+)	8	1917.5*	0.29(2)	560.5	4+	1			
			659.3*	0.29(4)	1823.7	5+	3			
			899.9*	0.71(7)	1583.1	4+	3			
2611.1	(7-)	4	215.2	0.38(2)	2395.7	(6-)	4			
			399.5	0.18(1)	2211.5	5-	4			
			528.3	0.35(9)	2083.1	(6+)	3			
			886.9*	0.29(4)	1724.2	6+	2			
			1531.3*	0.17(1)	1079.8	6+	1			
2668.9*	(7-)	5	211.7*	0.026(2)	2457.2	(6-)	5			
			392.4*	0.05(1)	2276.5	(5-)	5			
			944.7*	0.10(2)	1724.2	6+	2			
			308.0*	0.4(1)	2372.3	(7+)	3			
2680.4*	(8+)	3	597.3*	1.4(3)	2083.1	(6+)	3			
			956.2*	0.27(4)	1724.2	6+	2			
			646.1	2.6(2)	2036.3	7+	2			
2682.4	(9+)	2	961.0	0.71(4)	1721.4	8+	1			
			214.4*	0.8(1)	2483.0	(6+)	8			
2697.5*	(7+)	8	873.9*	0.5(1)	1823.7	5+	3			
			526.6	0.32(3)	2179.6	6-	6			
2706.4	8-	6	985.1	1.1(1)	1721.4	8+	1			
2863.8	(8-)	4	252.4	0.15(2)	2611.1	(7-)	4			
			468.2	0.18(1)	2395.7	(6-)	4			
			827.7	0.06(1)	2036.3	7+	2			
2866.0	(9)	7	561.3	3.7(2)	2304.7	(7)	7			
			1144.7	0.61(3)	1721.4	8+	1			
2932.1*	(8-)	5	263.2*	0.014(2)	2668.9	(7-)	5			
			474.9*	0.028(2)	2457.2	(6-)	5			
			895.8*	0.11(1)	2036.3	7+	2			
2935.3*	(7)		1855.5*	0.39(3)	1079.8	6+	1			
2953.8*	(8+)	8	256.3*	0.3(1)	2697.5	(7+)	8			
3004.9	(10+)	2	678.8	1.8(2)	2326.1	(8+)	2			
			1283.6	0.26(2)	1721.4	8+	1			
3008.7	(9+)	3	636.4	0.7(3)	2372.3	(7+)	3			
			972.6*	0.15(2)	2036.3	7+	2			
3050.2*	(6)		572.1*	0.18(2)	2478.1	(4)				
			1167.1*	0.40(3)	1883.1	5	7			
			1970.4*	0.07(2)	1079.8	6+	1			
			2489.7*	0.6(1)	560.5	4+	1			

TABLE I. (*Continued.*)

Initial level			Final level				
E_i (keV)	J^π	B	E_γ (keV)	I_γ	E_f (keV)	J^π	B
3130.0	(8)		825.3*	0.22(2)	2304.7	(7)	7
			950.4*	0.04(1)	2179.6	6-	6
			1408.6	0.44(2)	1721.4	8+	1
3145.0*	(9-)	4	281.4*	0.10(1)	2863.8	(8-)	4
			533.7*	0.09(1)	2611.1	(7-)	4
3254.5	(12+)	1	799.4	2.2(1)	2455.1	10+	1
3348.2*	(10+)	3	667.8*	0.6(3)	2680.4	(8+)	3
			1022.1*	0.11(2)	2326.1	(8+)	2
3358.1	10-	6	651.9	0.32(5)	2706.4	8-	6
			902.8	0.39(2)	2455.1	10+	1
3396.0	(11+)	2	713.6	1.4(1)	2682.4	(9+)	2
			940.4	0.20(2)	2455.1	10+	1
			486.2*	0.07(1)	2935.3	(7)	
3421.5*	(9)		1700.1*	0.09(1)	1721.4	8+	1
			688.6	1.3(1)	2866.0	(9)	7
3554.6	(11)	7	570.0	0.25(6)	3130.0	(8)	
3700.0	(10)		1244.9*	0.05(1)	2455.1	10+	1
			705.7*	0.3(1)	3008.7	(9+)	3
3765.4	(12+)	2	760.5	0.75(9)	3004.9	(10+)	2
4114.4	(12)	6	756.3	0.14(3)	3358.1	10-	6
4115.4	(14+)	1	860.9	0.58(6)	3254.5	(12+)	1
4183.2	(13+)	2	787.2	0.28(3)	3396.0	(11+)	2
4357.1	(13)	7	802.5	0.16(4)	3554.6	(11)	7
4625.9	(14+)	2	860.5	0.15(3)	3765.4	(12+)	2
4971.4*	(14)	6	(857.0)*		4114.4	(12)	6
5060.8	(16+)	1	945.4	0.08(1)	4115.4	(14+)	1
5061.5	(16+)	2	878.3	0.04(1)	4183.2	(13+)	2

(2) and 447.5 keV transition in band (2). Transitions directly feeding and indirectly feeding the 1475 keV 5^+ level of band (2) should be observed in both of these parts. In those two spectra, the 827.7 and 920.6 keV transitions decaying from band (4) to band (2), the 895.8 and 982.0 keV transitions decaying from band (5) to band (2), and 896.9 and 972.6 keV transitions decaying from band (3) to band (2) can be seen. In our data, there are global 896, 1014, 1039 keV contamination transitions in almost any coincidence spectra. The 895.8 and 896.9 keV transitions overlap in the spectra in Fig. 4. However, those two transitions are populating different states— 7^+ and 5^+ in band 2, respectively. The 895.8 keV transition can be identified from the 561–447 keV gated spectrum (not shown in the paper) with such 1 keV energy difference. The 1195.4 keV peak is a transition depopulating the 2671 keV level, as reported in previous β -decay work [32]. The 1180.7 keV transition is a new one decaying from the 2656 keV level to the 1475.2 keV level. The 2656 keV level was reported previously in Refs. [31,32]. Note that the 1180, 1195 keV transitions and 2656, 2671 keV levels are not placed in the ^{104}Mo level scheme in Fig. 1. This is because these levels do not belong to any band structure in the current work. The 808 keV contamination peak in part (a) comes from the coincidence of the 808 and 915 keV ground-state band transitions in ^{140}Ba , as reported in Refs. [33–35].

The 896 keV peak in Fig. 4 contains multiple components. Figure 5 provides more evidence for the new 896 keV transition directly feeding the 2036 keV level. In this spectrum, by gating on the 561.0 and 914.9 keV transitions, the 895.8 keV peak is clear. The 896.9 keV transition directly feeding the 1475 keV level is not in coincidence with this gate. Furthermore, the 1014 keV contamination transition almost disappears. Thus, the new 895.8 keV transition is real. One can also see the new 827.7 and 972.6 keV transitions.

Figure 6 provides more evidence for band (5) in ^{104}Mo . The spectrum in part (a) shows a gate on 192.0 and 982.0 keV. One can see the new 211.7, 263.2, and 474.9 keV transitions directly feeding and indirectly feeding the (6^-) level in band (5). Part (b) is a spectrum gated on 192.0 and 1022.4 keV transitions at the high-energy region. In this spectrum, one can see the new 648.4, 706.4, 846.4, 886.9, 944.7, 956.2, 1022.1, 1062.0, and 1085.7 keV transitions. The 846.4, 868.8, 997.2, and 1062.0 keV transitions are directly feeding the 4^+ state in band (2). The 648.4, 886.9, 944.7, and 956.2 keV transitions are directly populating the 6^+ state in band (2). The 1022.1 keV transition populates the (8^+) state in band (2). The 706.4 and 1085.7 keV transitions depopulate from nonband levels. Thus, they are not included in Fig. 1.

TABLE II. Level energies and γ -ray energies of ^{106}Mo obtained in the current work. Here, E_i , E_f , E_γ , I_γ and B correspond to initial level energy, final level energy, γ -ray energy, γ -ray intensity, and band number, respectively. The γ -ray intensities are normalized to the 171.5 keV one. New levels and transitions are labeled with an asterisk.

Initial level			Final level				
E_i (keV)	J^π	B	E_γ (keV)	I_γ	E_f (keV)	J^π	B
0.0	0+	1					
171.5	2+	1	171.5	100(5)	0.0	0+	1
522.0	4+	1	350.5	73(4)	171.5	2+	1
710.3	2+	2	538.8	8.8(4)	171.5	2+	1
			710.3	10.3(5)	0.0	0+	1
885.0	3+	2	174.7	0.24(5)	710.3	2+	2
			363.4	0.88(9)	522.0	4+	1
			713.5	21(1)	710.3	2+	2
1033.0	6+	1	511.0	46(2)	522.0	4+	1
1067.4	4+	2	182.2	0.29(6)	885.0	3+	2
			357.1	3.4(2)	710.3	2+	2
			545.4	6.5(4)	522.0	4+	1
			896.0	7.4(4)	171.5	2+	1
1149.7	(2+)	9	978.2	1.3(1)	171.5	2+	1
			1149.7	0.84(6)	0.0	0+	1
1306.6	5+	2	238.9	0.50(6)	1067.4	4+	2
			273.6	0.18(1)	1033.0	6+	1
			421.6	7.5(4)	885.0	3+	2
			784.6	9.3(5)	522.0	4+	1
1434.6	4+	3	367.2	0.44(9)	1067.4	4+	2
			549.5	3.8(2)	885.0	3+	2
			724.3	9.8(5)	710.3	2+	2
1536.1	(4+)	9	386.4	0.90(5)	1149.7	(2+)	9
			1014.1	1.8(1)	522.0	4+	1
			1364.6	1.8(1)	171.5	2+	1
1562.9	6+	2	256.4	0.61(6)	1306.6	5+	2
			495.5	7.5(4)	1067.4	4+	2
			530.0	3.0(2)	1033.0	6+	1
			1040.8	2.5(2)	522.0	4+	1
1657.5	5+	3	222.9	2.0(1)	1434.6	4+	3
			350.9	1.6(2)	1306.6	5+	2
			590.1	3.4(2)	1067.4	4+	2
			772.5	6.7(3)	885.0	3+	2
1687.9	8+	1	654.9	17(1)	1033.0	6+	1
1719.1	(3+)	10	834.1*	0.08(3)	885.0	3+	2
			1008.9	0.49(6)	710.3	2+	2
			1197.1*	0.11(2)	522.0	4+	1
			1547.6*	0.26(2)	171.5	2+	1
1817.0	(3-)	5	932.0	0.53(3)	885	3+	2
			1106.7	1.7(1)	710.3	2+	2
1867.6	7+	2	561.0	5.4(3)	1306.6	5+	2
			834.6	3.1(3)	1033.0	6+	1
1909.9	6+	3	252.2	1.3(1)	1657.5	5+	3
			475.3	2.4(2)	1434.6	4+	3
			603.3	2.3(3)	1306.6	5+	2
			842.6	2.6(2)	1067.4	4+	2
1936.6	(4-)	5	869.3	0.72(5)	1067.4	4+	2
			1051.6	1.1(1)	885.0	3+	2
			1414.6	0.12(3)	522.0	4+	1
1952.0	5-	4	294.5	0.19(3)	1657.5	5+	3
			517.4	5.7(3)	1434.6	4+	3
			884.6	<0.28	1067.4	4+	2

TABLE II. (*Continued.*)

Initial level			Final level							
E_i (keV)	J^π	B	E_γ (keV)	I_γ	E_f (keV)	J^π	B			
2014.1	(6+)	9	478.1	3.0(2)	1536.1	(4+)	9			
			981.1	0.70(5)	1033.0	6+	1			
			1492.1	1.3(1)	522.0	4+	1			
2090.2	(5-)	5	138.4	0.10(1)	1952.0	5-	4			
			153.7	0.26(3)	1936.6	(4-)	5			
			273.2	0.38(4)	1817.0	(3-)	5			
			783.7	1.5(1)	1306.6	5+	2			
			1022.7	2.2(1)	1067.4	4+	2			
			1057.0	0.22(2)	1033.0	6+	1			
			1568.2*	0.13(2)	522.0	4+	1			
2138.5*	4-	8	1616.5*	1.6(1)	522.0	4+	1			
2142.1	6-	4	190.2	2.3(1)	1952.0	5-	4			
			205.8	0.22(1)	1936.6	(4-)	5			
			232.2	0.91(7)	1909.9	6+	3			
			484.6	5.3(3)	1657.5	5+	3			
			835.5*	0.6(1)	1306.6	5+	2			
2146.6	(5-)	7	1113.6	0.87(7)	1033.0	6+	1			
			1624.6	0.88(6)	522.0	4+	1			
2157.9*	(5+)	10	438.8*	0.27(5)	1719.1	(3+)	10			
			851.3*	0.13(3)	1306.6	5+	2			
			1090.4*	0.61(6)	1067.4	4+	2			
			1635.9*	0.12(2)	522.0	4+	1			
2193.7	(8+)	2	505.9	1.1(1)	1687.9	8+	1			
			630.8	5.9(3)	1562.9	6+	2			
			1160.8	0.81(6)	1033.0	6+	1			
2198.2	4-	6	1676.2	0.8(2)	522.0	4+	1			
2199.5	7+	3	289.6	1.3(1)	1909.9	6+	3			
			542.0	1.8(1)	1657.5	5+	3			
			636.6	0.81(6)	1562.9	6+	2			
			892.9	0.79(7)	1306.6	5+	2			
			892.9	0.79(7)	1306.6	5+	2			
2275.9	(6-)	5	185.8	0.29(2)	2090.2	(5-)	5			
			324.2*	0.10(2)	1952.0	5-	4			
			339.3	0.76(5)	1936.6	(4-)	5			
			712.9	2.0(2)	1562.9	6+	2			
			969.4	1.4(1)	1306.6	5+	2			
			1242.9	0.50(4)	1033.0	6+	1			
			164.1*	0.05(1)	2138.5	4-	8			
2302.6	(5-)	8	1269.6	0.30(2)	1033.0	6+	1			
			1780.6	1.9(1)	522.0	4+	1			
			226.3	2.2(1)	2142.1	6-	4			
			278.3*	0.13(1)	2090.2	(5-)	5			
			416.6	2.9(2)	1952.0	5-	4			
2368.5	7-	4	458.6	2.3(2)	1909.9	6+	3			
			805.6*	0.67(6)	1562.9	6+	2			
			1335.7*	0.32(4)	1033.0	6+	1			
			1335.9*	0.29(5)	1033.0	6+	1			
			783.7	3.0(2)	1687.9	8+	1			
			193.6*	0.36(2)	2302.6	(5-)	8			
			298.0*	0.13(1)	2198.2	4-	6			
2471.6	10+	1	354.1*	0.12(2)	2142.1	6-	4			
			357.7*	0.61(4)	2138.5	4-	8			
			544.2*	0.08(1)	1952.0	5-	4			
			1189.6*	0.24(2)	1306.6	5+	2			
			1463.2*	0.08(1)	1033.0	6+	1			
			2496.2*	6-	8	193.6*	0.36(2)	2302.6	(5-)	8
			298.0*	0.13(1)	2198.2	4-	6			
			354.1*	0.12(2)	2142.1	6-	4			
357.7*	0.61(4)	2138.5	4-	8						
544.2*	0.08(1)	1952.0	5-	4						
1189.6*	0.24(2)	1306.6	5+	2						
1463.2*	0.08(1)	1033.0	6+	1						

TABLE II. (Continued.)

Initial level								Final level		
E_i (keV)	J^π	B	E_γ (keV)	I_γ	E_f (keV)	J^π	B			
2498.3	(7-)	5	129.8*	0.15(2)	2368.5	7-	4			
			222.2	0.67(5)	2275.9	(6-)	5			
			408.2	2.1(1)	2090.2	(5-)	5			
			810.4*	0.11(2)	1687.9	8+	1			
			935.3	0.84(7)	1562.9	6+	2			
2521.4	(8+)	3	321.9	1.2(1)	2199.5	7+	3			
			611.5	2.3(2)	1909.9	6+	3			
			958.6*	0.31(4)	1562.9	6+	2			
			2558.2	(9+)	2	690.6	2.4(3)	1867.6	7+	2
2560.9*	6-	6	870.4	0.29(3)	1687.9	8+	1			
			(362.7)*		2198.2	4-	6			
2565.1	(8+)	9	1527.9*	0.93(6)	1033.0	6+	1			
			551.0	2.7(2)	2014.1	(6+)	9			
			877.3	0.36(3)	1687.9	8+	1			
2565.6	(7-)	7	1532.3	0.64(8)	1033.0	6+	1			
			419.0	0.43(4)	2146.6	(5-)	7			
			877.9	0.25(2)	1687.9	8+	1			
2628.7	(8-)	4	1532.7	0.75(7)	1033.0	6+	1			
			260.3	1.5(1)	2368.5	7-	4			
			429.2	0.66(6)	2199.5	7+	3			
			486.6	4.2(2)	2142.1	6-	4			
2671.4*	(7+)	10	(761.1)*		1867.6	7+	2			
			513.5*	0.7(1)	2157.9	(5+)	10			
			1638.4*	0.26(5)	1033.0	6+	1			
2712.8	(7-)	8	216.6*	0.017(2)	2496.2	6-	8			
			410.2	0.66(4)	2302.6	(5-)	8			
			(436.9)*		2275.9	(6-)	5			
			1024.9	<0.17	1687.9	8+	1			
			1679.8	1.3(1)	1033.0	6+	1			
2746.2	(8-)	5	247.5	0.36(4)	2498.3	(7-)	5			
			470.2	2.3(2)	2275.9	(6-)	5			
			552.5*	0.12(6)	2193.7	(8+)	2			
			878.3	0.16(3)	1867.6	7+	2			
			1058.4	0.27(2)	1687.9	8+	1			
2877.4	(9+)	3	677.9	2.2(1)	2199.5	7+	3			
			2920.9*	(8)	552.1*	0.12(5)	2368.9	(6)		
2921.1	(9-)	4	1233.0*	0.29(2)	1687.9	8+	1			
			1887.9*	0.18(2)	1033.0	6+	1			
			292.4	0.55(3)	2628.7	(8-)	4			
			552.6	3.2(2)	2368.5	7-	4			
2949.7	(10+)	2	756.0	2.7(3)	2193.7	(8+)	2			
			1261.9	<0.08	1687.9	8+	1			
2976.9*	8-	8	264.1*	0.17(1)	2712.8	(7-)	8			
			480.7*	0.87(5)	2496.2	6-	8			
			1109.3*	0.07(1)	1867.6	7+	2			
			1289.0*	0.05(1)	1687.9	8+	1			
3040.7	(9-)	5	294.1	0.22(3)	2746.2	(8-)	5			
			542.4	1.9(1)	2498.3	(7-)	5			
			3080.4*	8-	6	519.5*	0.47(3)	2560.9	6-	6
3131.6	(9-)	7	1392.5*	0.18(4)	1687.9	8+	1			
			566.0	0.77(8)	2565.6	(7-)	7			
			1443.7	0.80(6)	1687.9	8+	1			
3183.9	(10+)	9	618.8	1.8(2)	2565.1	(8+)	9			
3237.8	(10-)	4	316.6	0.17(1)	2921.1	(9-)	4			
			609.1	1.5(2)	2628.7	(8-)	4			
3249.9*	(9+)	10	578.5*	0.6(1)	2671.4	(7+)	10			
			1562*	<0.03	1687.9	8+	1			

TABLE II. (*Continued.*)

Initial level			Final level				
E_i (keV)	J^π	B	E_γ (keV)	I_γ	E_f (keV)	J^π	B
3253.0	(9-)	8	276.1*	0.08(1)	2976.9	8-	8
			540.2	0.73(4)	2712.8	(7-)	8
			1565.1	0.22(5)	1687.9	8+	1
3264.7	(10+)	3	743.3	1.0(2)	2521.4	(8+)	3
3349.6	(10-)	5	308.9	0.23(2)	3040.7	(9-)	5
			603.4	1.5(1)	2746.2	(8-)	5
			720.9*	0.15(2)	2628.7	(8-)	4
3369.0	12+	1	897.4	0.6(1)	2471.6	10+	1
3369.2	(11+)	2	811.0	0.38(6)	2558.2	(9+)	2
3591.3	(11-)	4	353.5	0.10(2)	3237.8	(10-)	4
			670.2	0.79(6)	2921.1	(9-)	4
			622.7*	0.34(9)	2976.9	8-	8
3682.2	(11+)	3	804.8	0.20(3)	2877.4	(9+)	3
3706.6	(11-)	5	357.0	0.17(2)	3349.6	(10-)	5
			665.9	0.79(7)	3040.7	(9-)	5
			650.0*	<0.1	3080.4	8-	6
3730.4*	(10-)	6	650.0*	<0.1	3080.4	8-	6
(3786.5)*	(12+)	9	(602.6)*		3183.9	(10+)	9
3809.5	(12+)	2	859.8	0.35(5)	2949.7	(10+)	2
3842.0	(11-)	7	710.4	<0.7	3131.6	(9-)	7
3882.0*	(11+)	10	632.1*	0.09(3)	3249.9	(9+)	10
3927.9	(11-)	8	674.9	0.28(4)	3253.0	(9-)	8
3945.1	(12-)	4	353.8	0.027(6)	3591.3	(11-)	4
			707.3	0.65(8)	3237.8	(10-)	4
			742.5*	0.29(4)	3349.6	(10-)	5
4092.1*	(12-)	5	742.5*	0.29(4)	3349.6	(10-)	5
(4133.2)	(12+)	3	(868.5)		3264.7	(10+)	3
4291.0	(13+)	2	921.8	0.03(1)	3369.2	(11+)	2
4361.7	14+	1	992.7	0.10(2)	3369.0	12+	1
4370.3	(13-)	4	779.0	0.12(2)	3591.3	(11-)	4
(4751.2)	(14-)	4	(806.1)		3945.1	(12-)	4
(4756.6)	(14+)	2	(947.1)		3809.5	(12+)	2

Figure 7 shows coincidence spectra by gating on (a) 1163.8 and 368.5 keV transitions and (b) 509.8 and 1022.4 keV transitions in ^{104}Mo . One can see transitions feeding the 1724 keV level in these two spectra. The 886.9 and 956.2 keV new transitions are clear in these spectra. The 944.7 keV transition is relatively weak in these spectra. However, these two spectra together with Fig. 6(b) and other coincidence spectra, not included here, provide sufficient evidence for this 944.7 keV new transition. Figure 8 depicts the co-

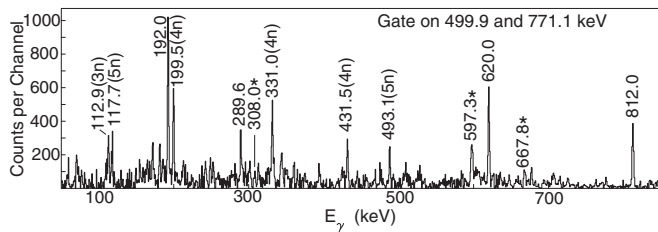


FIG. 3. Partial γ -ray coincidence spectra by gating on 499.9 and 771.1 keV transitions in ^{104}Mo . New transitions are labeled with an asterisk. Fission partner transitions are labeled with neutron evaporation numbers. Here, 3n, 4n, and 5n denote ^{145}Ba , ^{144}Ba , and ^{143}Ba , respectively.

incidence spectra by gating on the 1022.4 keV transition in ^{104}Mo and 199.5 keV transition from the fission partner ^{144}Ba in part (a), and 402.5 and 620.0 keV transitions in ^{104}Mo in

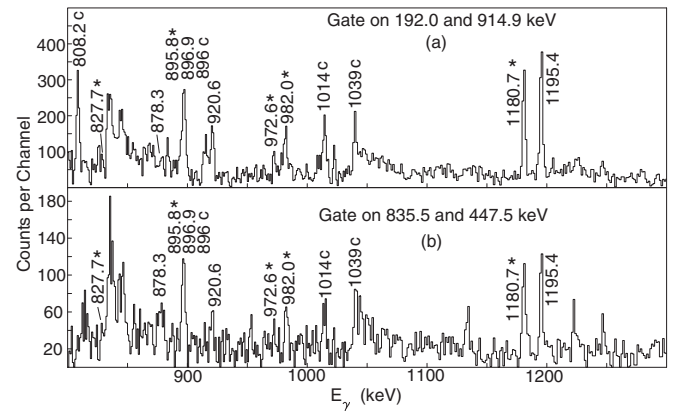


FIG. 4. Partial γ -ray coincidence spectra by gating on (a) 192.0 and 914.9 keV transitions and (b) 835.5 and 447.5 keV transitions in ^{104}Mo . New transitions are labeled with an asterisk. Contamination transitions are labeled with a "c." Note that the 1180 and 1195 keV transitions are not placed in the level scheme.

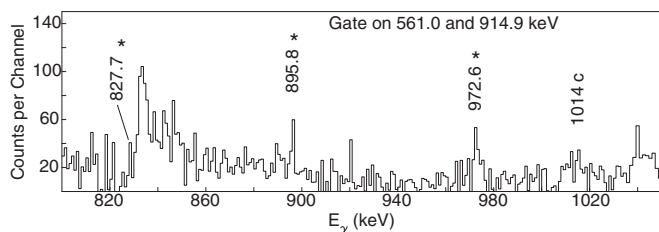


FIG. 5. Partial γ -ray coincidence spectrum by gating on 561.0 and 914.9 keV transitions in ^{104}Mo . New transitions are labeled with an asterisk. Contamination transitions are labeled with a “c.”

part (b). One can see the new 1062.0 keV transition populating the 1214 keV level in these two spectra. These two spectra and Fig. 6 as well as other coincidence spectra, not included here, show convincing evidence for the new 1062.0 keV linking transition.

Band (6) in ^{104}Mo was reported in Ref. [31]. Band (7) in ^{104}Mo was reported in Refs. [30,31,36]. This band (6) is reassigned as possible negative parity. In our data, we do not see the J to $J-2$ transitions in Ref. [31]. In detail, the even spin levels in band (6) only decay to the same spin ground-state band levels, e.g., the transition from the 2179.6 keV 6^- level to the 560.5 4^+ keV transition is not seen in the data.

The new band (8) in ^{104}Mo is tentatively assigned as a three-phonon γ -vibrational band. This is because of the proposed tentatively assigned 6^+ band head based on decay pattern and energy spacing. Also, this band only decays to the two-phonon γ -vibrational band. However, this band could be another quasiparticle band. More work is needed to understand the structure and configuration of this band.

B. ^{106}Mo spectra

In ^{106}Mo , a band with a (5^+) band head at 2302.9 keV was reported in Ref. [31]. In the current work, the even spin levels of this band have been identified. The band head of the even

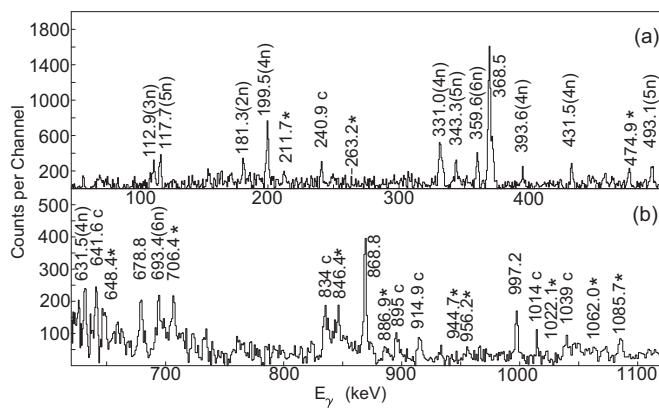


FIG. 6. Partial γ -ray coincidence spectra by gating on (a) 192.0 and 982.0 keV transitions and (b) 192.0 and 1022.4 keV transitions in ^{104}Mo . New transitions are labeled with an asterisk. Contamination transitions are labeled with a “c.” Note that the 706.4 and 1085.7 keV transitions in part (b) are not placed in the level scheme. Here, 2n, 3n, 4n, 5n, and 6n denote ^{146}Ba to ^{142}Ba , respectively.

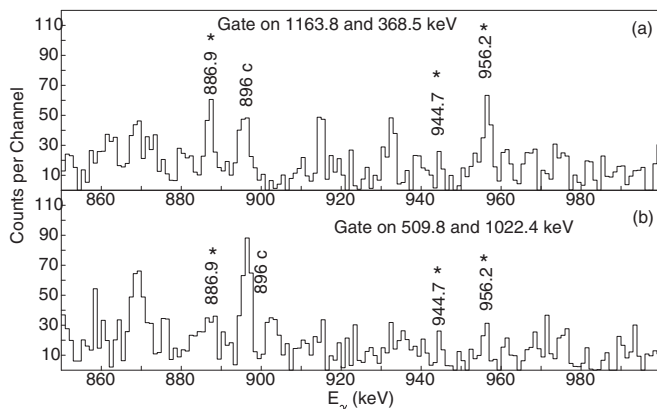


FIG. 7. Partial γ -ray coincidence spectra by gating on (a) 1163.8 and 368.5 keV transitions and (b) 509.8 and 1022.4 keV transitions in ^{104}Mo . New transitions are labeled with an asterisk.

spin of band 8 is reassigned as the 4^- at the 2138.5 keV level based on the absence of the energetically favored decay to the 2^+ state and the 2302.6 keV level as 5^- . Likewise, from a similar decay pattern, band (6) is assigned as a 4^- band. Figures 9 and 10 give evidence for these band structures. In Fig. 9, from a summation of three gates on the ground-state band in ^{106}Mo , one can see the 1269.4 and 1679.8 keV transitions previously reported in Ref. [31] decaying from band (8) to the ground-state band. The new 1289.0, 1463.2, and 1616.5 keV transitions decaying from band (8) to the ground-state band are also seen in this spectrum. Other 1355.7, 1355.9, 1359.5, 1527.9, 1633.4, and 1635.9 keV new transitions are also seen in this spectrum. The 1359.5 and 1633.4 keV transitions are real, but not placed in the level scheme in Fig. 2. The 1351 and 1569 keV transitions from ^{144}Ba were identified previously in Refs. [34,37]. Figures 10(a) and 10(b) show evidence for the $M1$ and $E2$ transitions in band (8). In Fig. 10(a) with a gate on 1780.6, 350.5, and 171.5 keV transitions, the new 193.6 (6^- to 5^-), 216.6 (7^- to 6^-), and 264.1 keV (8^-

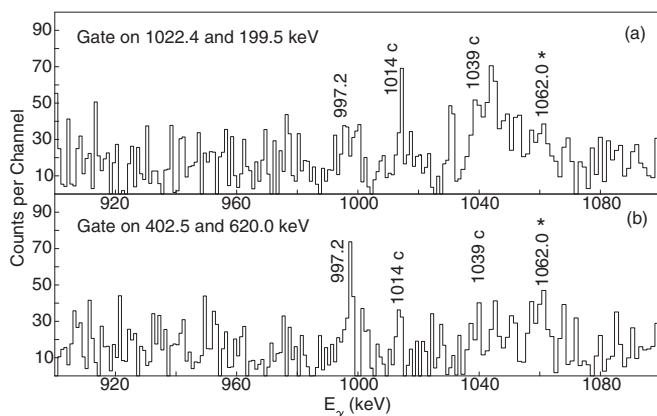


FIG. 8. Partial γ -ray coincidence spectra by gating on the (a) 1022.4 keV transition in ^{104}Mo and 199.5 keV transition from the fission partner ^{144}Ba , and (b) 402.5 and 620.0 keV transitions in ^{104}Mo . New transitions are labeled with an asterisk. Contamination transitions are labeled with a “c.”

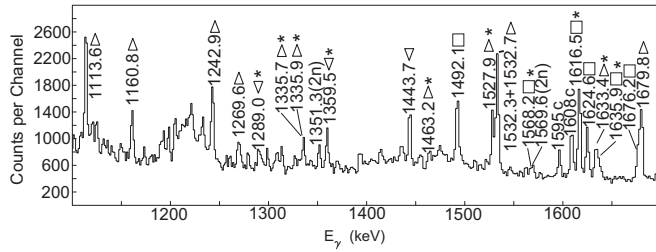


FIG. 9. Partial γ -ray coincidence spectra by summing three gates on 171.5 and 350.5 keV, 350.5 and 511.0 keV, and 511.0 and 654.9 keV transitions in the ground-state band of ^{106}Mo . Here, \square represents the transitions populating the 4^+ level of the ground-state band, Δ denotes the transitions populating the 6^+ state of the ground-state band, and ∇ represents the transitions populating the 8^+ state of the ground-state band. New transitions are labeled with asterisks. Contamination transitions are labeled with a “c.” Here, 2n represents transitions in ^{144}Ba . Note that the 1359.5 and 1633.4 keV transitions are not placed in the level scheme.

to 7^-) $M1$ transitions in band (8) can be seen. In part (b), by gating on the 1616.5, 350.5, and 171.5 keV transitions, the new 164.1, 193.6, and 216.6 keV $M1$ transitions, as well as the new 357.7, 480.7, and 622.7 keV $E2$ transitions, in band (8) can be seen.

The evidence for band (6) is shown in Fig. 11. By gating on the 1527.9 keV linking transitions from band (6) to ground-state band (1), and the 350.5 and 511.0 keV transitions in band (1), the new 519.5 and 650.0 keV $E2$ transitions in band (6) can be observed in the spectrum. The Ba fission partners’ transitions as well as the 171.5 keV ground-state band transition are also labeled in the figure. The 654.9 keV transition is proposed to be a contamination because the peak is much weaker than the 171.5 keV. It comes from the coincidence of 350.5, 511.0, and the background around the 1527.9 keV region.

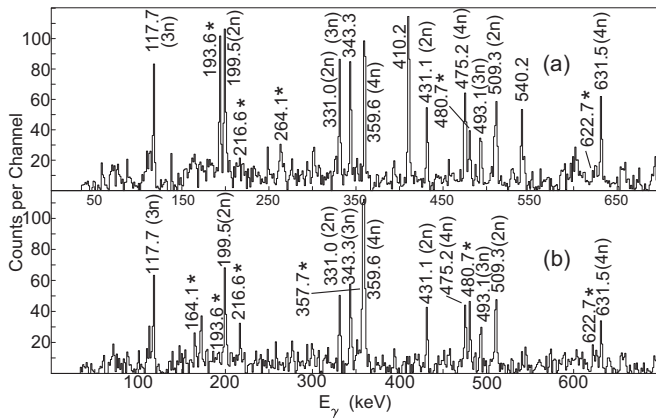


FIG. 10. Partial γ -ray coincidence spectra in ^{106}Mo (a) by gating on the 1780.6, 350.5, and 171.5 keV transitions, and (b) by gating on the 1616.5, 350.5, and 171.5 keV transitions. New transitions are labeled with an asterisk. Fission partner transitions are labeled with neutron evaporation numbers. Namely, 2n, 3n, and 4n denote ^{144}Ba , ^{143}Ba , and ^{142}Ba , respectively.

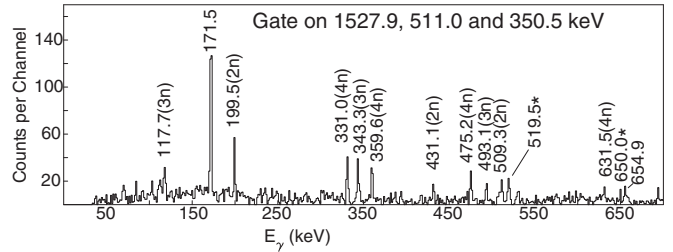


FIG. 11. Partial γ -ray coincidence spectra by gating on 1527.9, 511.0, and 350.5 keV transitions in ^{106}Mo . New transitions are labeled with an asterisk. Fission partner transitions are labeled with neutron evaporation numbers. Here, 2n, 3n, 4n, and 5n denote ^{144}Ba , ^{143}Ba , ^{142}Ba , and ^{141}Ba , respectively.

Some of the linking transitions from band (10) to band (1) are shown in Fig. 9. Figure 12 gives evidence for the $E2$ transitions in band (10). The new 513.5, 578.5, and 632.1 keV can be seen in this figure with the 438.8, 1008.8, and 538.8 keV gated spectrum.

C. Angular correlations

Angular correlation measurements have been made to determine the spins and parities in $^{104,106}\text{Mo}$. For ^{104}Mo , as shown in Fig. 13, the two results generally agree with theoretical $4(D)4(Q)2$ and $5(D)5(Q)3$ values, which are $A_2 = 0.196$, $A_4 = 0$ and $A_2 = 0.186$, $A_4 = 0$, respectively. These measurements confirm the assignments of the 4^- and 5^- states in band (4). The band head of band (5) is tentatively argued as 5^- according to the decay pattern and level energy differences. The $5^- \rightarrow 4^+$ transition is seen, but not the energetically favored $5^- \rightarrow 3^+$, which should be seen if parity is positive and similarly for the spin 6, 7, and 8 levels. The angular correlation of the 1323–368 keV cascade in ^{104}Mo shows evidence for a 5 spin of the 1883 keV level. As a comparison, Ref. [31] assigned tentative 5^- for this level without any further discussions. However, the A_2 , A_4 values of the 1323–368 keV angular correlation is within 1 sigma error of a theoretical pure dipole. Therefore, because of the large uncertainty, the result does not show clear evidence for the parity assignment. In this paper, we did not assign the parity of this band-head 1883 level. If the band 7 in ^{104}Mo is the odd spin partner of band 6 with the same configuration, the parity of band 7 would be negative.

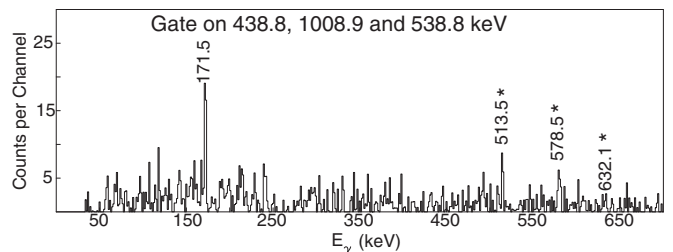


FIG. 12. Partial γ -ray coincidence spectra by gating on 438.8, 1008.9, and 538.8 keV transitions in ^{106}Mo . New transitions are labeled with an asterisk.

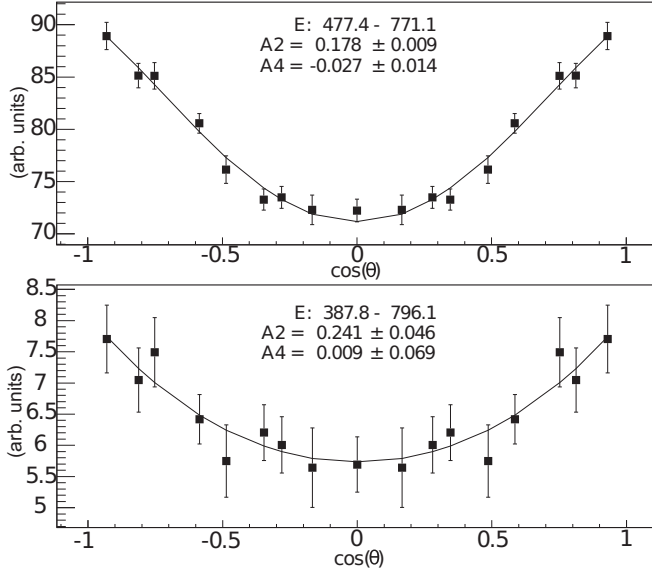


FIG. 13. The γ - γ angular correlations of 477.4–771.1 keV (top) and 387.8–796.1 keV (bottom) in ^{104}Mo .

For ^{106}Mo , the spins and parities of the 2^+ to 8^+ levels in the γ band, and the 4^+ to 7^+ levels in the $\gamma\gamma$ band, were confirmed by the directional correlations from oriented states (DCO) in Ref. [23]. These assignments of the 2^+ to 7^+ levels in the γ band were also confirmed by the γ - γ angular correlation measurements [38]. As shown in Table III, the 1434.6 keV 4^+ band head of the γ - γ band is confirmed by the current angular correlation measurements. The spin and parity of the 7^+ state of the $\gamma\gamma$ band is confirmed by the 542.0–772.5 keV cascade. The 517.4–724.3 keV cascade angular correlation agrees with a pure $5^-(D)4^+(Q)2^+$ pattern. This measurement confirms the 1952.0 keV 5^- level in band (4) of ^{106}Mo . The measurement of the 190.2–517.4 keV cascade can give the $E2/M1$ mixing ratio of the 190.2 keV transition (from the 2142.0 keV level to the 1952.0 keV level) in band (4) by assuming a pure $E1$ 517.4 keV transition. The two values of -0.6 and -1.9 correspond to 26% quadrupole vs 74% dipole and 78% quadrupole vs 22% dipole for the 190.2 keV transition, respectively, and $B(M1;190.2,6^- \rightarrow 5^-)/B(E2;190.2,6^- \rightarrow 5^-)$ values for 0.070 and 0.0070 $(\mu_N/eb)^2$, respectively. For the 226.3–485.0 keV cascade, the measured A_2 is a little larger than the maximum value for the $7^-(Q/D)6^-(D)5^+$. Therefore, only one value of the $E2/M1$ mixing ratio is obtained. The -1.0 value corresponds to 50% quadrupole vs 50% dipole, and 0.036 $(\mu_N/eb)^2$ for $B(M1;226.3,7^- \rightarrow 6^-)/B(E2;226.3,7^- \rightarrow 6^-)$ in band (4).

III. TPSTM CALCULATIONS

Bands (4) and (5) in $^{104,106}\text{Mo}$ are proposed to be the chiral partners. As seen in Figs. 14 and 15, the chiral bands in $^{104,106}\text{Mo}$ exhibit small energy splitting between odd and even spin levels, and the same rotational response $I(\omega)$. The energy differences of the doublet bands are quite small and almost constant with increasing spin, being about half of the

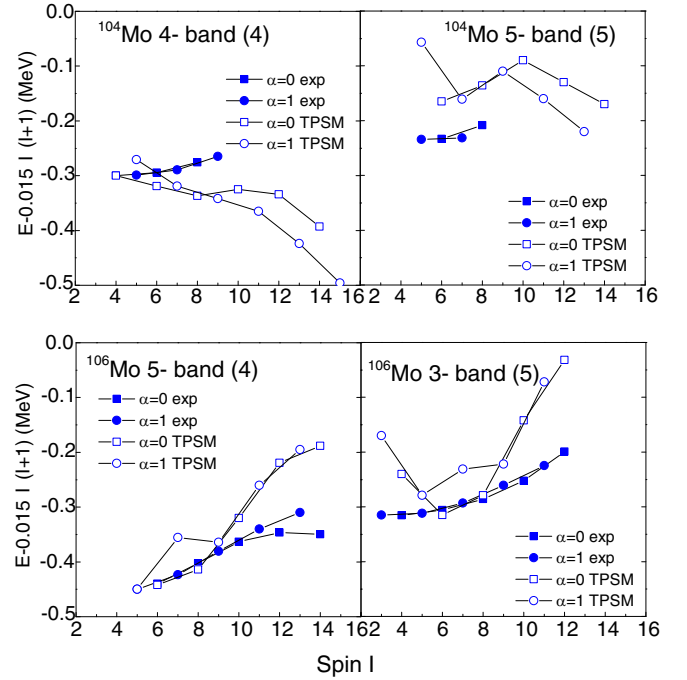


FIG. 14. Comparison of the measured energy levels $E - 0.015 * I * (I + 1)$ vs spin (I) for $^{104,106}\text{Mo}$ with TPSTM calculated values. Data for ^{106}Mo have been taken from Ref. [9] and the current work. Here, E is normalized to the band 4 band-head energies in $^{104,106}\text{Mo}$, respectively.

differences in ^{104}Mo compared to ^{106}Mo , as shown in Fig. 16. These are the characteristics of very soft chiral vibrations. We have performed theoretical calculations for the chiral doublet bands in these nuclei.

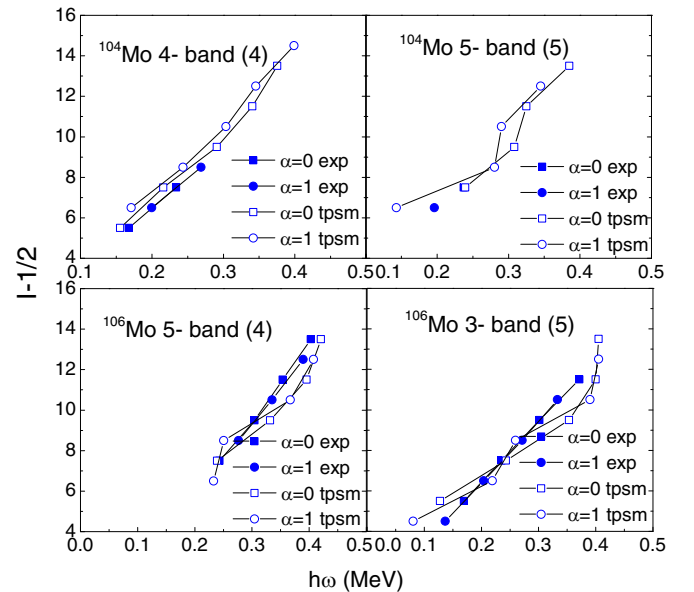


FIG. 15. Plots of $I - 0.5$ vs rotational frequency $\hbar\omega = [E(I) - E(I - 2)]/2$ for $^{104,106}\text{Mo}$ from the experiment and TPSTM calculations.

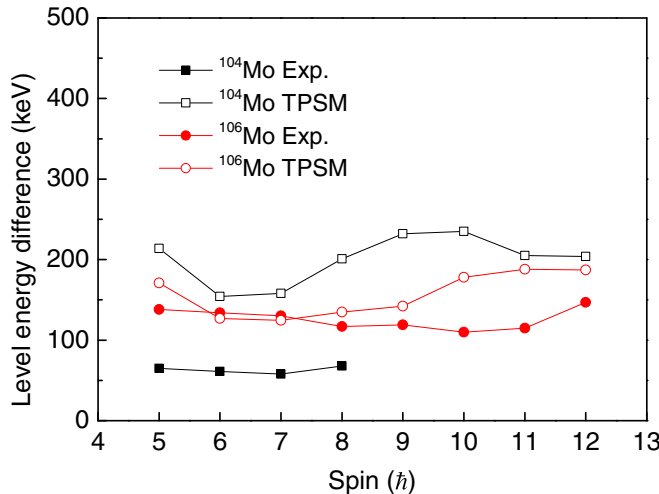


FIG. 16. Level energy differences $E_5(I) - E_4(I)$ between chiral doublet bands in $^{104,106}\text{Mo}$ from the experiment and TPMSM calculations.

In recent years, the triaxial projected shell model (TPSM) approach has been shown to reproduce the high-spin properties of deformed nuclei quite well [39–42]. In this approach, the model space is composed of three major oscillator shells for neutrons and protons with pairing plus quadrupole-quadrupole as the model Hamiltonian. In the original version of the model, quasiparticle excitations were restricted to the last major oscillator shell and, due to this limitation, it was possible to study only positive parity bands in even-even systems. In order to investigate the negative parity band structures, populated in the present experimental work, the TPM approach has been generalized by considering two-quasiparticle excitations from two major oscillator shells with one neutron (proton) in one oscillator shell, and the second neutron (proton) in the other oscillator shell having opposite parity. More details on this extension shall be provided in separate papers [39].

By using the extended approach, numerical calculations have been performed for the negative parity bands observed in $^{104,106}\text{Mo}$ with the following parameter set: $\varepsilon = 0.24$, $\gamma = 20^\circ$ (104), 36° (106). The other parameters are quoted in our earlier study of the positive parity bands in [43].

The calculated levels in band 4 and band 5 in $^{104,106}\text{Mo}$, respectively, are shown in Fig. 17. The energies are normalized to the band 4 band head of these two nuclei, respectively. Experimental data are also included for comparison. In ^{104}Mo , the calculations of band 4 and band 5 have regular energy spacing of the rotational bands and can reproduce the experimental data. In ^{106}Mo , the calculated 3^- level of band 5 is 50 keV below the 4^- state of this band. In comparison, the experiment 3^- , 4^- , and 5^- states have regular energy spacing and orders.

The calculated TPM energies for two nuclei are included in Fig. 14 along with the observed energies. Note that the 12^- state in band 5 of ^{106}Mo is different from the previous work in Refs. [9,44]. The TPM approach reproduces the observed energies well (note the expanded energy scale).

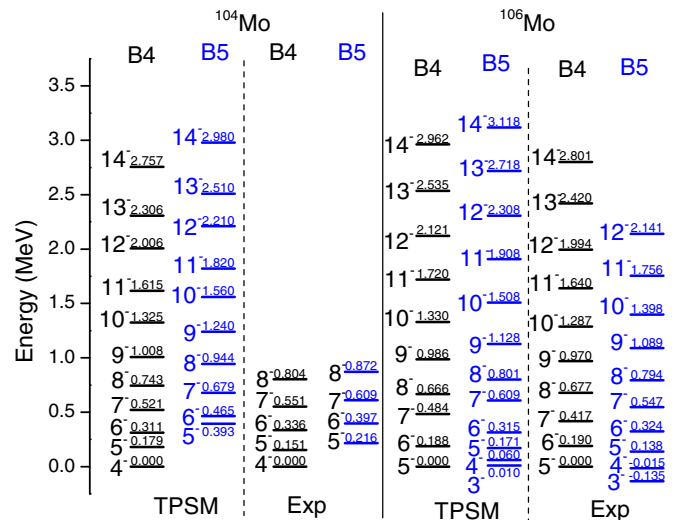


FIG. 17. Comparison of the TPM calculated energy level to the experimental data. Energies are normalized to the 4^- state of band 4 of ^{104}Mo and 5^- state of band 4 of ^{106}Mo , respectively.

At large angular momentum, the TPM overestimates the energies, which is seen in the angular momentum vs frequency plots in Fig. 15, as a too small slope for ^{106}Mo . For ^{104}Mo , the calculations trend towards underestimation for band (4) and they overestimate band (5) at low spins, but may also be trending towards underestimation at higher spins. We attribute the discrepancy to the assumption of a fixed deformation in the TPM. Figure 16 displays that the key feature of chiral partner bands—the small distance between states of the same I —is reasonably in agreement with the TPM calculations.

The calculated $J^{(1)}$ moments of inertia are also compared with the experimental data from the current work. As shown in Fig. 18, the calculations show staggering at low spin, which differs from the experimental data. However, the staggering of $J^{(1)}$ can be generally reproduced for they are centered

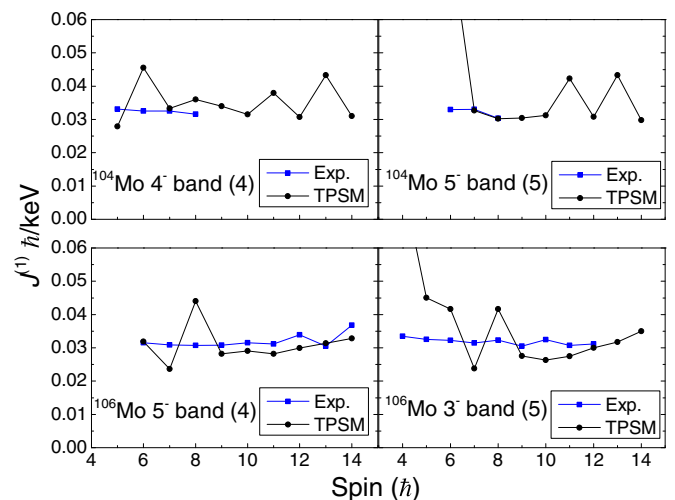


FIG. 18. Comparison of the $J^{(1)}$ moments of inertia in bands 4 and 5 between TPM calculations and experimental data.

TABLE III. Angular correlation of the $^{104,106}\text{Mo}$ nuclei. Here, D represents a dipole transition and Q represents a quadrupole transition. The δ represents the $E2/M1$ mixing ratios. Other angular correlations from Ref. [38] are indicated by an asterisk.

Cascade	A_2, A_4 Expt.		A_2, A_4 Theor.		Decay pattern	δ
^{104}Mo						
*620.0 (812.0 \rightarrow 192.0)	—	192.0 (192.0 \rightarrow 0.0)	-0.15(3), 0.4(1)		2 ⁺ (Q/D)2 ⁺ (Q)0 ⁺	9, (0.6)
*835.5 (1027.5 \rightarrow 192.0)	—	192.0 (192.0 \rightarrow 0.0)	-0.19(2), -0.12(4)		3 ⁺ (Q/D)2 ⁺ (Q)0 ⁺	50, (-0.15)
*654.0 (1214.5 \rightarrow 560.5)	—	368.5 (560.5 \rightarrow 192.0)	-0.16(1), 0.16(2)		4 ⁺ (Q/D)4 ⁺ (Q)2 ⁺	7
*914.9 (1475.2 \rightarrow 560.5)	—	368.5 (560.5 \rightarrow 192.0)	-0.10(1), -0.6(2)		5 ⁺ (Q/D)4 ⁺ (Q)2 ⁺	30
*956.6 (2036.3 \rightarrow 1079.8)	—	519.3 (1079.8 \rightarrow 560.5)	-0.01(3), 0.07(5)		7 ⁺ (Q/D)6 ⁺ (Q)4 ⁺	0.1, (7)
*961.0 (2682.4 \rightarrow 1721.4)	—	641.6 (1721.4 \rightarrow 1079.8)	0.10(6), -0.15(9)		9 ⁺ (Q/D)8 ⁺ (Q)6 ⁺	3, (0.31)
1322.6 (1883.1 \rightarrow 560.5)	—	368.5 (560.5 \rightarrow 192.0)	-0.10(3), -0.02(5)	-0.07, 0	5(D)4 ⁺ (Q)2 ⁺	
477.4 (2060.6 \rightarrow 1583.1)	—	771.1 (1583.1 \rightarrow 812.0)	0.18(1), -0.03(1)	0.20, 0	4 ⁻ (D)4 ⁺ (Q)2 ⁺	
387.8 (2211.5 \rightarrow 1823.7)	—	796.1 (1823.7 \rightarrow 1027.5)	0.24(5), 0.01(7)	0.19, 0	5 ⁻ (D)5 ⁺ (Q)3 ⁺	
^{106}Mo						
*538.8 (710.3 \rightarrow 171.5)	—	171.5 (171.5 \rightarrow 0.0)	-0.18(2), 0.27(8)		2 ⁺ (Q/D)2 ⁺ (Q)0 ⁺	6.2, (0.65)
*713.5 (885.0 \rightarrow 171.5)	—	171.5 (171.5 \rightarrow 0.0)	-0.08(1), -0.08(3)		3 ⁺ (Q/D)2 ⁺ (Q)0 ⁺	6.1, (-0.01)
*545.4 (1067.5 \rightarrow 522.0)	—	350.5 (522.0 \rightarrow 171.5)	-0.19(1), 0.11(2)		4 ⁺ (Q/D)4 ⁺ (Q)2 ⁺	(2.1)
*784.6 (1306.6 \rightarrow 522.0)	—	350.5 (522.0 \rightarrow 171.5)	0.023(7), -0.05(1)		5 ⁺ (Q/D)4 ⁺ (Q)2 ⁺	4.4
*530.0 (1562.9 \rightarrow 1033.0)	—	511.0 (1033.0 \rightarrow 522.0)	-0.07(2), 0.04(3)		6 ⁺ (Q/D)6 ⁺ (Q)4 ⁺	1.1, (5)
*834.6 (1867.6 \rightarrow 1033.0)	—	511.0 (1033.0 \rightarrow 522.0)	0.08(3), -0.08(5)		7 ⁺ (Q/D)6 ⁺ (Q)5 ⁺	3.2, 0.26
724.3 (1434.6 \rightarrow 710.3)	—	710.3 (710.3 \rightarrow 0.0)	0.11(1), 0.02(2)	0.10, 0	4 ⁺ (Q)2 ⁺ (Q)0 ⁺	
542.0 (2199.5 \rightarrow 1657.5)	—	772.5 (1657.5 \rightarrow 885.0)	0.11(5), -0.04(7)	0.10, 0	7 ⁺ (Q)5 ⁺ (Q)3 ⁺	
517.4 (1952.0 \rightarrow 1434.6)	—	724.3 (1434.6 \rightarrow 710.3)	-0.08(1), -0.01(2)	-0.07, 0	5 ⁻ (D)4 ⁺ (Q)2 ⁺	
190.2 (2142.1 \rightarrow 1952.0)	—	517.4 (1952.0 \rightarrow 1434.6)	0.26(2), -0.03(3)		6 ⁻ (Q/D)5 ⁻ (D)4 ⁺	-0.6, -1.9
226.3 (2368.5 \rightarrow 2142.1)	—	484.6 (2142.1 \rightarrow to 1657.5)	0.29(3), 0.05(5)		7 ⁻ (Q/D)6 ⁻ (D)5 ⁺	-1.0

around the experimental data. At medium spin, both the experimental data and calculated results are flat. The calculations also predict large staggering at high spin for ^{104}Mo without experimental data for comparison.

We have also evaluated the transition probabilities using the TPSM wave functions. These have been calculated using free values for g_l and for g_s , with an attenuation factor of 0.85, i.e., $g_l^\pi = 1$, $g_l^v = 0$, $g_s^\pi = 5.59 \times 0.85$, and $g_s^v = -3.83 \times 0.85$. Comparison of the experimental and the calcu-

lated ratios of in-band $B(M1)/B(E2)$ transition probabilities for $^{104,106}\text{Mo}$ are depicted in Fig. 19. Here, $B(M1)$ depicts $\Delta I = 1$ chiral in-band reduced transition probabilities, while $B(E2)$ depicts $\Delta I = 2$ chiral in-band reduced transition probabilities. It is observed from this figure that the numerical results obtained from TPSM with the present parameter set are generally in agreement with the observed data. The calculation also presents a drop of the $B(M1)/B(E2)$ ratios in band 4 of ^{104}Mo .

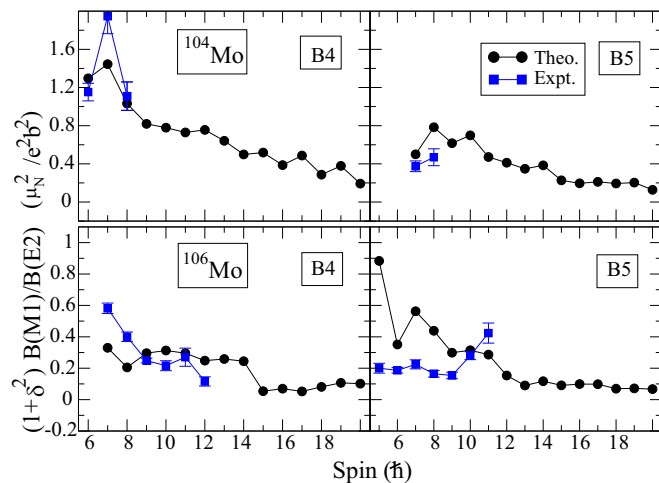


FIG. 19. Comparison of the measured $B(M1)(\mu_N^2)/B(E2)(e^2b^2) * (1 + \delta^2)$ shown as a square with TPSM calculated values shown as a circle for $^{104,106}\text{Mo}$ nuclei. Here, $B(M1)$ depicts $\Delta I = 1$ chiral in-band reduced transition probabilities, while $B(E2)$ depicts $\Delta I = 2$ chiral in-band reduced transition probabilities.

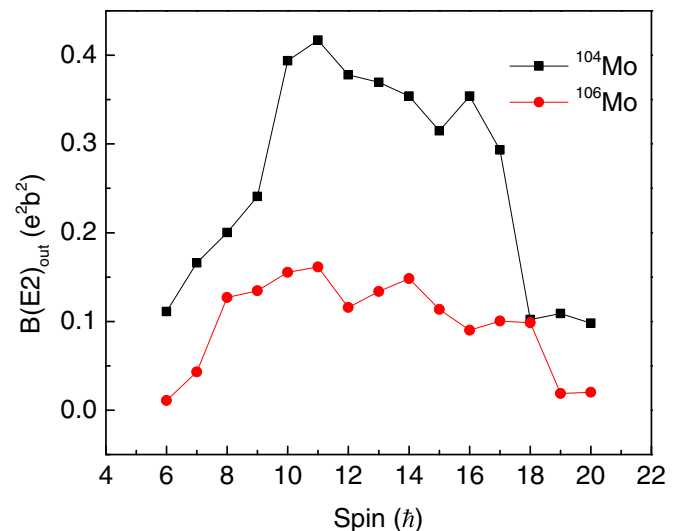


FIG. 20. $B(E2, I \rightarrow I - 1)_{\text{out}}$ values for the transitions connecting bands 5 and 4 from the TPSM calculation.

TABLE IV. Comparison of the intensities of the expected $I \rightarrow I - 1$ transitions connecting bands 5 and 4 between TPSM calculations and experimental limit. Here, $B(E2)_{\text{out}}$ corresponds to the calculated values for the $I \rightarrow I - 1$ transitions connecting bands 5 and 4, and $B(E2)_{\text{in}}$ corresponds to the calculated values for the $I \rightarrow I - 2$ transitions in band 5. Here, the $M1$ and $E2$ mixing of the $I \rightarrow I - 1$ transitions is considered in order to deduce the correct values for the intensities.

Spin	$B(E2)_{\text{out}}/B(E2)_{\text{in}}$	E_γ (keV)	$I_{\gamma\text{-theo}}$	$I_{\gamma\text{-exp}}$
^{104}Mo				
7	0.725	273.2	0.006	
8	0.677	321.0	0.0038	
^{106}Mo				
7	0.294	356.2	0.26	<0.2
8	0.766	377.7	0.20	<0.15
9	0.745	412.0	0.12	<0.1
10	0.801	428.5	0.082	
11	0.813	468.8	0.038	
12	0.634	500.8	0.020	<0.02

Figure 20 shows the $B(E2, I \rightarrow I - 1)_{\text{out}}$ values for the transitions connecting bands 5 and 4. They are highly collective, about 40–90% of the stretched intraband values $B(E2, I \rightarrow I - 2)_{\text{in}}$ at most of the spins. The high collectivity indicates that the two bands are related by reorientation of the triaxial charge density with respect to the total angular momentum vector. This is in contrast to the possibility that the two bands represent just two different quasineutron configurations, in which case the $B(E2, I \rightarrow I - 1)_{\text{out}}$ would be only of the single-particle value. The enhancement strongly supports the interpretation of the bands as chiral partners.

From the TPSM calculated $B(E2)_{\text{out}}$ and $B(E2)_{\text{in}}$ ratios, combined with the $E2_{\text{in}}$ transition intensities measured from the experimental data, one can calculate the expected $E2(I \rightarrow I - 1)_{\text{out}}$ intensities. The results are shown in Table IV. The $M1$ and $E2$ mixing of the $I \rightarrow I - 1$ transitions is considered in order to deduce the correct values for the intensities. Although those connecting transitions between chiral doublets cannot be clearly identified, some upper limits are given for some of the cases with very weak evidence. Generally speaking, the calculated intensities are too weak to be seen (at least a magnitude smaller than the other strong transitions populating the same state). Some of the theoretical expectations are a little bit above the experimental upper limit.

The analysis of the wave functions provides further support. As in the tilted axis cranking calculations of Ref. [9], it is found that the main components come from two configurations that contain one $h_{11/2}$ quasineutron and one from a pseudo-spin pair of ($d_{5/2}g_{7/2}$) quasineutrons. The partner bands differ by the weights of the components with different angular momentum K that are projected from these two two-quasineutron configurations. This indicates that the partner bands are related by a reorientation of the total angular momentum.

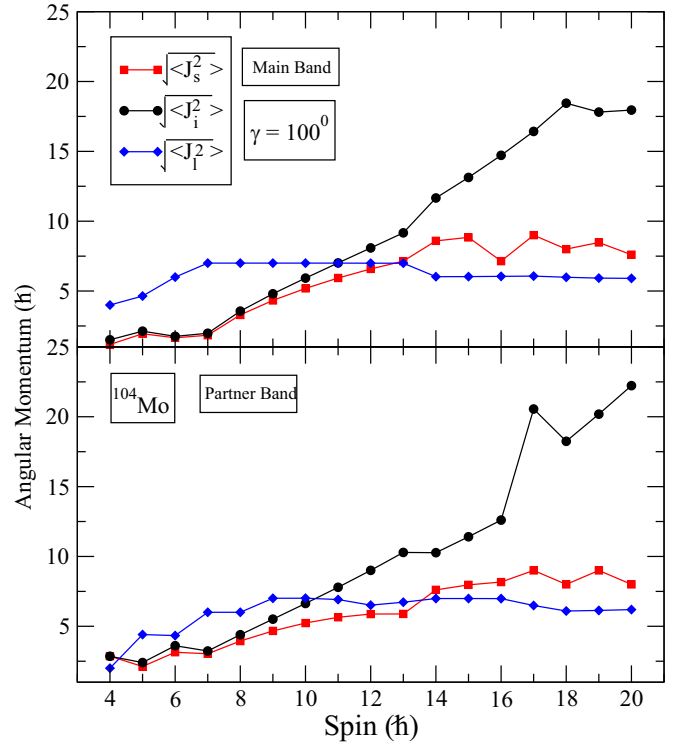


FIG. 21. The expectation values of the squared angular momentum components for the main band ($B4$) and partner band ($B5$) for the total nucleus in ^{104}Mo . The value $\gamma = 100^\circ$ was used in order to mitigate small errors caused by the truncation of the configuration space in the TPSM code. The change $\gamma = 20^\circ \rightarrow 100^\circ$ only interchanges the intrinsic order of the axes in the code.

To specify this observation, we have calculated the expectation values of the square of the components of total angular momentum, which are obtained as follows:

$$\langle IM | J_i^2 | IM \rangle = \sum_{KkK'k'} f_{Kk} f_{K'k'} \langle IK'' | J_i^2 | IK \rangle N_{K''kK'k'}. \quad (1)$$

The sum runs over K , the projections of the total angular momentum, and k , the label of the quasiparticle configurations. The coefficients f_{Kk} are the weights of the projected quasiparticle configurations, which form the nonorthogonal basis of the TPSM, $N_{K''kK'k'}$ are the norm overlaps between the basis states, and $\langle IK'' | J_i^2 | IK \rangle$ are the standard matrix elements between states of good angular momentum [45].

In Fig. 21, the three components of the angular momentum are different from zero, which indicates a chiral geometry. The three components are about the same for both the main (band 4) and the partner (band 5) bands, which indicates that they, respectively, represent the even or odd linear combinations of the left- and right-handed versions of the structure illustrated in Fig. 21. For both chiral doublet bands, the collective core angular momentum mainly aligns along the intermediate axis (i axis) because it has the largest moment of inertia. Note that there is a sharp change at $I = 17$ for the

^{104}Mo partner band. The reason for this discontinuity is the crossing of the four-neutron configuration having aligned two neutrons with the ground-state negative parity band. This band crossing is delayed as compared to the positive parity band in even-even systems since the lowest orbital is blocked for the negative parity band with one neutron occupying the intruder orbital. More details on the band crossings' features in negative parity bands shall be provided in a separate theoretical paper.

In summary, new levels and transitions have been identified in neutron-rich $^{104,106}\text{Mo}$. Bands (4) and (5) in these nuclei are proposed as soft chiral vibrational doublet bands. These doublet rotational bands in ^{104}Mo show similar behavior to those in ^{106}Mo , but exhibit smaller separation energies. The theoretical calculations support the assignments of these newly observed bands as soft chiral doublet bands built on

the $h_{11/2}$ quasineutron and a pseudo-spin pair of ($d_{5/2}g_{7/2}$) quasineutrons.

ACKNOWLEDGMENTS

The work at Vanderbilt University and Lawrence Berkeley National Laboratory is supported by the U.S. Department of Energy under Grant No. DE-FG05-88ER40407 and Contract No. DE-AC03-76SF00098. The work at Tsinghua University was supported by the National Natural Science Foundation of China under Grant No. 11175095. The work at JINR was supported by the Russian Foundation for Basic Research Grant No. 08-02-00089 and by the INTAS Grant No. 03-51-4496. S.F. acknowledges support by the U.S. Department of Energy under Grant No. DF-FG02-95ER40934.

-
- [1] S. Frauendorf and J. Meng, *Nucl. Phys. A* **617**, 131 (1997).
 [2] S. Y. Wang *et al.*, *Phys. Lett. B* **703**, 40 (2011).
 [3] T. Koike *et al.*, *Intl. J. Mod. Phys. E* **20**, 520 (2011).
 [4] C. Vaman, D. B. Fossan, T. Koike, K. Starosta, I. Y. Lee, and A. O. Macchiavelli, *Phys. Rev. Lett.* **92**, 032501 (2004).
 [5] P. Joshi *et al.*, *Phys. Lett. B* **595**, 135 (2004).
 [6] J. Timár *et al.*, *Phys. Lett. B* **598**, 178 (2004).
 [7] J. A. Alcántara-Núñez *et al.*, *Phys. Rev. C* **69**, 024317 (2004).
 [8] P. Joshi *et al.*, *Eur. Phys. J. A* **24**, 23 (2005).
 [9] S. J. Zhu *et al.*, *Eur. Phys. J. A* **25**, 459 (2005).
 [10] P. Joshi, M. P. Carpenter, D. B. Fossan, T. Koike, E. S. Paul, G. Rainovski, K. Starosta, C. Vaman, and R. Wadsworth, *Phys. Rev. Lett.* **98**, 102501 (2007).
 [11] T. Suzuki, G. Rainovski, T. Koike, T. Ahn, M. P. Carpenter, A. Costin, M. Danchev, A. Dewald, R. V. F. Janssens, P. Joshi, C. J. Lister, O. Möller, N. Pietralla, T. Shinozuka, J. Timár, R. Wadsworth, C. Vaman, and S. Zhu, *Phys. Rev. C* **78**, 031302(R) (2008).
 [12] Y. X. Luo *et al.*, *Phys. Lett. B* **670**, 307 (2009).
 [13] J. Sethi *et al.*, *Phys. Lett. B* **725**, 85 (2013).
 [14] D. Tonev, M. S. Yavahchova, N. Goutev, G. de Angelis, P. Petkov, R. K. Bhowmik, R. P. Singh, S. Muralithar, N. Madhavan, R. Kumar, M. Kumar Raju, J. Kaur, G. Mohanto, A. Singh, N. Kaur, R. Garg, A. Shukla, T. K. Marinov, and S. Brant, *Phys. Rev. Lett.* **112**, 052501 (2014).
 [15] E. O. Lieder, R. M. Lieder, R. A. Bark, Q. B. Chen, S. Q. Zhang, J. Meng, E. A. Lawrie, J. J. Lawrie, S. P. Bvumbi, N. Y. Kheswa, S. S. Ntshangase, T. E. Madiba, P. L. Masiteng, S. M. Mullins, S. Murray, P. Papka, D. G. Roux, O. Shirinda, Z. H. Zhang, P. W. Zhao, Z. P. Li, J. Peng, B. Qi, S. Y. Wang, Z. G. Xiao, and C. Xu, *Phys. Rev. Lett.* **112**, 202502 (2014).
 [16] N. Rather, P. Datta, S. Chattopadhyay, S. Rajbanshi, A. Goswami, G. H. Bhat, J. A. Sheikh, S. Roy, R. Palit, S. Pal, S. Saha, J. Sethi, S. Biswas, P. Singh, and H. C. Jain, *Phys. Rev. Lett.* **112**, 202503 (2014).
 [17] K. Starosta, T. Koike, C. J. Chiara, D. B. Fossan, D. R. LaFosse, A. A. Hecht, C. W. Beausang, M. A. Caprio, J. R. Cooper, R. Krucken, J. R. Novak, N. V. Zamfir, K. E. Zyranski, D. J. Hartley, D. L. Balabanski, J. Y. Zhang, S. Frauendorf, and V. I. Dimitrov, *Phys. Rev. Lett.* **86**, 971 (2001).
 [18] S. Zhu, U. Garg, B. K. Nayak, S. S. Ghugre, N. S. Pattabiraman, D. B. Fossan, T. Koike, K. Starosta, C. Vaman, R. V. F. Janssens, R. S. Chakrawarthy, M. Whitehead, A. O. Macchiavelli, and S. Frauendorf, *Phys. Rev. Lett.* **91**, 132501 (2003).
 [19] E. Grodner, J. Srebrny, A. A. Pasternak, I. Zalewska, T. Morek, C. Droste, J. Mierzejewski, M. Kowalczyk, J. Kownacki, M. Kisielinski, S. G. Rohozinski, T. Koike, K. Starosta, A. Kordyasz, P. J. Napiorkowski, M. Wolinska-Cichocka, E. Ruchowska, W. Płociennik, and J. Perkowski, *Phys. Rev. Lett.* **97**, 172501 (2006).
 [20] S. Mukhopadhyay, D. Almeded, U. Garg, S. Frauendorf, T. Li, P. V. Madhusudhana Rao, X. Wang, S. S. Ghugre, M. P. Carpenter, S. Gros, A. Hecht, R. V. F. Janssens, F. G. Kondev, T. Lauritsen, D. Seweryniak, and S. Zhu, *Phys. Rev. Lett.* **99**, 172501 (2007).
 [21] D. L. Balabanski, M. Danchev, D. J. Hartley, L. L. Riedinger, O. Zeidan, J. Y. Zhang, C. J. Barton, C. W. Beausang, M. A. Caprio, R. F. Casten, J. R. Cooper, A. A. Hecht, R. Krucken, J. R. Novak, N. V. Zamfir, and K. E. Zyranski, *Phys. Rev. C* **70**, 044305 (2004).
 [22] P. L. Masiteng *et al.*, *Phys. Lett. B* **719**, 83 (2013).
 [23] A. Guessous, N. Schulz, W. R. Phillips, I. Ahmad, M. Bentaleb, J. L. Durell, M. A. Jones, M. Leddy, E. Lubkiewicz, L. R. Morss, R. Piepenbring, A. G. Smith, W. Urban, and B. J. Varley, *Phys. Rev. Lett.* **75**, 2280 (1995).
 [24] A. Guessous, N. Schulz, M. Bentaleb, E. Lubkiewicz, J. L. Durell, C. J. Pearson, W. R. Phillips, J. A. Shannon, W. Urban, B. J. Varley, I. Ahmad, C. J. Lister, L. R. Morss, K. L. Nash, C. W. Williams, and S. Khazrouni, *Phys. Rev. C* **53**, 1191 (1996).
 [25] S. Frauendorf, *Rev. Mod. Phys.* **73**, 463 (2001).
 [26] V. Dimitrov *et al.*, *AIP Conf. Proc.* **656**, 151 (2003).
 [27] D. C. Radford, *Nucl. Instrum. Methods Phys. Res., Sect. A* **361**, 297 (1995).
 [28] A. V. Daniel *et al.*, *Nucl. Instrum. Methods B* **262**, 399 (2007).
 [29] J. H. Hamilton *et al.*, *Prog. Part. Nucl. Phys.* **35**, 635 (1995).
 [30] H. Hua, C. Y. Wu, D. Cline, A. B. Hayes, R. Teng, R. M. Clark, P. Fallon, A. Goergen, A. O. Macchiavelli, and K. Vetter, *Phys. Rev. C* **69**, 014317 (2004).
 [31] E. F. Jones *et al.*, *Phys. Atom. Nuclei* **69**, 1198 (2006).

- [32] B. D. Kern *et al.*, *Z. Phys. A* **306**, 161 (1982).
- [33] S. J. Zhu *et al.*, *Chin. Phys. Lett.* **14**, 569 (1997).
- [34] W. Urban *et al.*, *Nucl. Phys. A* **613**, 107 (1997).
- [35] Ts. Venkova *et al.*, *Eur. Phys. J. A* **34**, 349 (2007).
- [36] L. M. Yang *et al.*, *Chin. Phys. Lett.* **18**, 24 (2001).
- [37] S. J. Zhu, E. H. Wang, J. H. Hamilton, A. V. Ramayya, Y. X. Liu, N. T. Brewer, Y. X. Luo, J. O. Rasmussen, Z. G. Xiao, Y. Huang, G. M. Ter-Akopian, and T. Oganessian, *Phys. Rev. Lett.* **124**, 032501 (2020).
- [38] J. M. Eldridge *et al.*, *Eur. Phys. J. A* **54**, 15 (2018).
- [39] S. Jehangir *et al.* (unpublished)
- [40] J. A. Sheikh, G. H. Bhat, Y. Sun, G. B. Vakil, and R. Palit, *Phys. Rev. C* **77**, 034313 (2008).
- [41] J. A. Sheikh, G. H. Bhat, Y. X. Liu, F. Q. Chen, and Y. Sun, *Phys. Rev. C* **84**, 054314 (2011).
- [42] C. L. Zhang, G. H. Bhat, W. Nazarewicz, J. A. Sheikh, and Y. Shi, *Phys. Rev. C* **92**, 034307 (2015).
- [43] G. H. Bhat *et al.*, *Nucl. Phys. A* **947**, 127 (2016).
- [44] S. J. Zhu *et al.*, *Chin. Phys. C* **33**, 145 (2009).
- [45] J. A. Sheikh *et al.*, *Phys. Scr.* **91**, 063015 (2016).